ADVANCED ENERGY MATERIALS
www.advenergymat.de

Sodium-Doped Tin Sulfide Single Crystal: A Nontoxic Earth-Abundant Material with High Thermoelectric Performance

Hong Wu, Xu Lu, Guoyu Wang, Kunling Peng, Hang Chi, Bin Zhang, Yongjin Chen, Chengjun Li, Yanci Yan, Lijie Guo, Ctirad Uher, Xiaoyuan Zhou, and Xiaodong Han**

Lead-free tin sulfide (SnS), with an analogous structure to SnSe, has attracted increasing attention because of its theoretically predicted high thermoelectric performance. In practice, however, polycrystalline SnS performs rather poorly as a result of its low power factor. In this work, bulk sodium (Na)-doped SnS single crystals are synthesized using a modified Bridgman method and a detailed transport evaluation is conducted. The highest *zT* value of ≈1.1 is reached at 870 K in a 2 at% Na-doped SnS single crystal along the *b*-axis direction, in which high power factors (2.0 mW m^{-1} K^{-2} at room temperature) are realized. These high power factors are attributed to the high mobility associated with the single crystalline nature of the samples as well as to the enhanced carrier concentration achieved through Na doping. An effective single parabolic band model coupled with first-principles calculations is used to provide theoretical insight into the electronic transport properties. This work demonstrates that SnS-based single crystals composed of earth-abundant, low-cost, and nontoxic chemical elements can exhibit high thermoelectric performance and thus hold potential for application in the area of waste heat recovery.

To alleviate worldwide energy shortages and environmental issues caused by the excessive use of fossil fuel-generated energy, the development of green energy technology has become imperative. One solution has been to use thermoelectric (TE) devices, which can directly convert waste heat into electricity without generating any additional pollution.[1–3] In general, TE materials that contain inexpensive earth-abundant and nontoxic elements are the most interesting applications.[4,5] The conversion efficiency for a TE material is determined by the dimensionless figure of merit (zT), defined as $zT = S^2 \rho^{-1} \kappa^{-1} T$, where S is the Seebeck coefficient, ρ is the electrical resistivity, T is the absolute temperature, and κ is the total thermal conductivity consisting of the lattice part (κ_L) and the electronic part (κ_e).[6] Some of these parameters (S, ρ, and κ_e), however, are mutually interdependent and strongly coupled by way of the carrier concentration, making it difficult to attain high TE performance (zT) without making some compromise. Fortunately, in the past decade, several general strategies have been developed to achieve high zT in various materials.[7,8] Lowering the lattice thermal conductivity (κ_L), which is relatively independent of other parameters, is a comparatively easy method. Other well-documented methods for enhancing phonon scattering include nanostructuring,[9–11] dislocations,[12,13] point defects,[14–17] and strong lattice anharmonicity.[18–20] Additional strategies to boost the power factor ($S^2\rho^{-1}$) include carrier concentration optimization,[21,22] band convergence,[23,24] and creating band resonance levels.[25]

Typically, practical TE materials are polycrystalline structures with grain boundaries that help to maintain a low lattice thermal conductivity but inevitably also degrade the charge carrier mobility. Recently, bulk SnSe[26–30] and In_4Se_3[31] single crystals have attracted increasing amounts of attention. The layered structure and strong lattice anharmonicity of these materials cause ultralow lattice thermal conductivity, independent of grain boundary phonon scattering. Therefore, such single crystalline compounds are expected to yield superior performance as both high mobility and low lattice thermal conductivity can be maintained simultaneously. For instance, the ultrahigh zT of

H. Wu, Prof. X. Lu, K. L. Peng, C. J. Li, Y. C. Yan, L. J. Guo, Prof. X. Y. Zhou
College of Physics
Chongqing University
Chongqing 401331, P. R. China
E-mail: xiaoyuan2013@cqu.edu.cn
H. Wu, Prof. G. Y. Wang
Chongqing Institute of Green and Intelligent Technology
Chinese Academy of Sciences
Chongqing 400714, P. R. China
H. Wu, Prof. G. Y. Wang
University of Chinese Academy of Sciences
Beijing 100044, P. R. China
Dr. H. Chi, Prof. C. Uher
Department of Physics
University of Michigan
Ann Arbor, MI 48109, USA
Dr. B. Zhang, Prof. X. Y. Zhou
Analytical and Testing Center of Chongqing University
Chongqing 401331, P. R. China
Y. J. Chen, Prof. X. D. Han
Beijing Key Laboratory of Microstructure and Property of Advanced Materials
Beijing University of Technology
Beijing 100024, P. R. China
E-mail: xdhan@bjut.edu.cn

DOI: 10.1002/aenm.201800087

 © 2018 WILEY-VCH Verlag GmbH & Co. KGaA, Weinheim

≈2.6 at 923 K for SnSe single crystals along the *b*-axis has been achieved.[26]

The analogous crystal structure of SnS to SnSe has suggested that potentially it should also have ultralow lattice thermal conductivity. Indeed, the first-principles calculations predict a high Seebeck coefficient (S) and low thermal conductivity (κ) for SnS.[32,33] The recent study using polycrystalline SnS samples was rather disappointing in its outcome as it resulted in a relatively low zT value of 0.65 at 850 K,[34] suffering chiefly from the low power factors of the polycrystalline samples. The prospect of achieving significantly higher power factors with single crystal samples of SnS and the lack of information regarding their transport properties have motivated us to perform a comprehensive study of the TE performance of single-crystalline forms of SnS.

In this work, we grew bulk SnS single crystals using a modified Bridgman method. The denotation of three principle crystallography directions is shown in Figure S1a (Supporting Information). Like other single crystal, the transport properties of SnS exhibit strong anisotropy, which will be demonstrated in the following section. We focus on the favorable direction (*b* direction) first and cover the details of anisotropy in the last section. The hole concentration is significantly improved by sodium (Na) doping on the sites of tin (Sn). Meanwhile, the carrier mobility is high compared with SnS polycrystalline samples because of the lack of grain boundary scattering. As a result, we achieved a high power factor (2.0 mW m^{-1} K^{-2}) at room temperature. We maintained the power factor above 0.75 mW m^{-1} K^{-2} at elevated temperatures for the 2 at% Na-doped SnS along the *b*-axis direction, which enabled a high zT value of ≈1.1 at 870 K. Furthermore, an analysis based on the effective single parabolic band (SPB) model coupled with first-principles calculations proved that the high power factor primarily resulted from the secondary heavy valence band contributing to transport.

Crystal structure characterizations: **Figure 1**a shows X-ray diffraction (XRD) of $Sn_{1-x}Na_xS$ (x = 0, 0.001, 0.01, 0.02, 0.03, and 0.04) single crystals obtained on the (100) cleavage surface, similar to SnSe single crystals.[26,27] Additionally, we collected powder XRD patterns, which are shown in Figure S1b (Supporting Information) for phase identification and crystalline parameter determination. All major reflection peaks can be indexed to those of PDF#014-0620, indicating the crystal structure of the $Sn_{1-x}Na_xS$ single crystals belongs to the *Pnma* space group and no secondary phases are present. Results of Rietveld refinement for undoped and Na-doped SnS crystals are shown in Table S1 (Supporting Information). We performed scanning transmission electron microscopy high-angle annular dark field (STEM-HAADF) and energy-dispersive X-ray spectrum (EDS) mapping on the $Sn_{0.98}Na_{0.02}S$ crystal to obtain its detailed structural analysis. As illustrated by the structure model (Figure 1b), the double Sn–S planes are linked by the van der Waals force along the [100] direction, which was confirmed by the HAADF image (Figure 1c). Thus, it is easy to cleave SnS single crystals (both doped and undoped) along the (100) planes, as illustrated in Figure 1b. The HAADF image and the corresponding EDS mapping with atomic-scale resolvable structural identification are shown in Figure 1d–g. As expected, Sn and S atoms are located on different columns of the [001] projection. In the

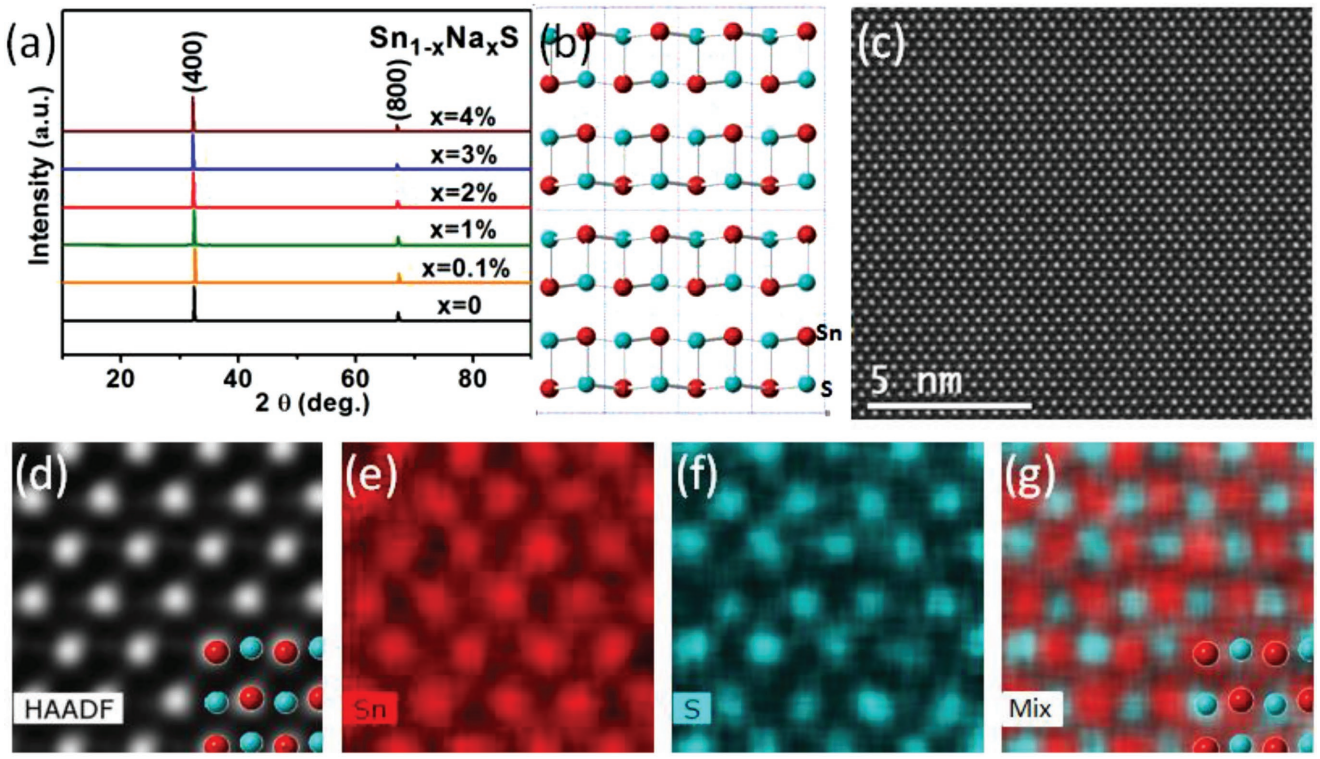

Figure 1. Structural characterization of $Sn_{1-x}Na_xS$ single crystals. a) XRD patterns. b) The atomic arrangement of SnS (Pnma) projected along the [001] direction. c) The [001] HAADF image of $Sn_{0.98}Na_{0.02}S$. d–g) STEM-EDS mapping of $Sn_{0.98}Na_{0.02}S$ with the HAADF image and the corresponding elemental mappings. A structure schematic is attached at (d) the bottom right corner of the HAADF image and at (g) the mixture mapping.

© 2018 WILEY-VCH Verlag GmbH & Co. KGaA, Weinheim

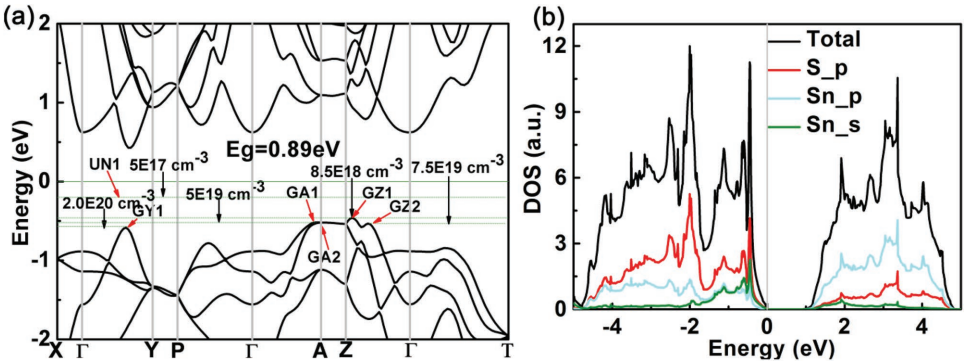

Figure 2. a) The calculated electronic band structure of SnS and carrier density as a function of the Fermi level. b) The total and partial density of states for the pristine SnS.

HAADF images, Sn columns appear as bright dots because of their large atomic number (50), whereas S columns are dimmer, as further confirmed by EDS mappings. A schematic of the atomic structure is attached at the bottom right corner of the HAADF image (Figure 1d) and at the bottom right corner of the combined EDS mapping (Figure 1g). Finally, note that because of the small content and weak EDX signals, we do not present the EDS mapping graphic of Na.

Electronic transport properties: To better understand the physical nature of electronic transport properties, we calculated the band structure of SnS (*Pnma* space group) along the high symmetry directions. As shown in **Figure 2**a, the calculated bandgap of SnS is ≈0.89 eV, which agrees with the results of previous calculations[35] and is smaller than that which we obtained experimentally from optical measurements (≈1.1 eV; see Figure S6 in the Supporting Information), because of the intrinsic underestimation of bandgap sizes in the density functional theory (DFT) calculations. We assumed that the slight (≈10%) underestimation of the bandgap would not affect the band edge morphology, as clarified in previous reports for SnSe.[27] As shown in Figure 2a, the valence band maximum was situated at GZ1 (0.0, 0.0, 0.448) along the Γ-Z symmetry direction, whereas the position of the second valence band maximum was situated at GA1 (0.466, 0.0, 0.466) along the Γ-A direction. The energy difference between these two valence band extrema was ≈0.055 eV (see **Table 1**), which was comparable to that of SnSe (≈0.057 eV).[27] Consequently, we expected that the second band could play an important role in the electronic transport when the structure was sufficiently doped. To clarify variations of the Fermi level with respect to the Na-doping content in SnS, which determined the number of carrier pockets participating in the carrier transport, we applied the BoltzTrap code[36,37] to calculate the corresponding carrier concentration when the Fermi level reached different extreme points. Figure 2a shows that the Fermi level pushed down into the second carrier pockets (GA1) when the carrier concentration reached ≈5.0×10^{19} cm^{-3} at 300 K, suggesting that multiple carrier pockets contributed to the carrier transport, which is beneficial for the enhancement of the power factor. In addition, the density of states (DOS) for pristine SnS is displayed in Figure 2b, which clearly shows that the DOS near the valence band edge principally originated from the contribution of p-orbitals of S atoms.

As listed in Table 1, we calculated the band effective masses at GZ1 and GA1; the method of calculations is provided in the Supporting Information. The result of calculations at each specific extreme point yielded anisotropic effective masses, with the effective mass along the k_x direction being larger than the mass in the other two directions (k_y and k_z), because of the quasi-laminar and highly anisotropic structure of SnS. This was consistent with a previous report,[35] in which the effective masses of the first band (m^*_{kx} = 2.63 m_e, m^*_{ky} = 0.32 m_e, and m^*_{kz} = 0.20 m_e) and those of the second band (m^*_{kx} = 8.48 m_e, m^*_{ky} = 0.29 m_e, and m^*_{kz} = 0.54 m_e) were reported. Hence, the DOS effective mass of the second band (≈3.063 m_e) was three times larger than that of the first band (≈0.971 m_e), indicating a potentially enhanced Seebeck coefficient benefiting from the presence of such heavy band.

It is assumed that the bandgap (≈1.1 eV) is large enough for SnS to exhibit the parabolic character at the band edges. In addition, the Hall mobility decreased with increasing temperature, following the relationship of $\mu \approx T^{-1.5}$ (**Figure 3**c). This suggested that the charge carriers mainly were scattered by acoustic phonons. Thereby, we are able to use an equivalent SPB model

Table 1. Effective masses of SnS obtained by fitting the band structure. The extremum position of the top valence band and the offset of each extremum from the first valence band maximum (VBM) are also listed in this Table.

Valence band tops	VBM [eV]	m_{kx} [m_e]	m_{ky} [m_e]	m_{kz} [m_e]	m_c* [m_e]	m_b* [m_e]	m_d* [m_e]
GZ1	0.0	3.051	0.338	0.222	0.385	0.612	0.971
GA1	0.055	6.781	0.740	0.358	0.698	1.215	3.063
GA2	0.059	20.01	6.270	0.415	1.145	3.734	9.409
GZ2	0.071	1.278	0.798	0.233	0.474	0.619	0.983
GY1	0.123	0.319	0.291	0.169	0.240	0.251	0.397

© 2018 WILEY-VCH Verlag GmbH & Co. KGaA, Weinheim

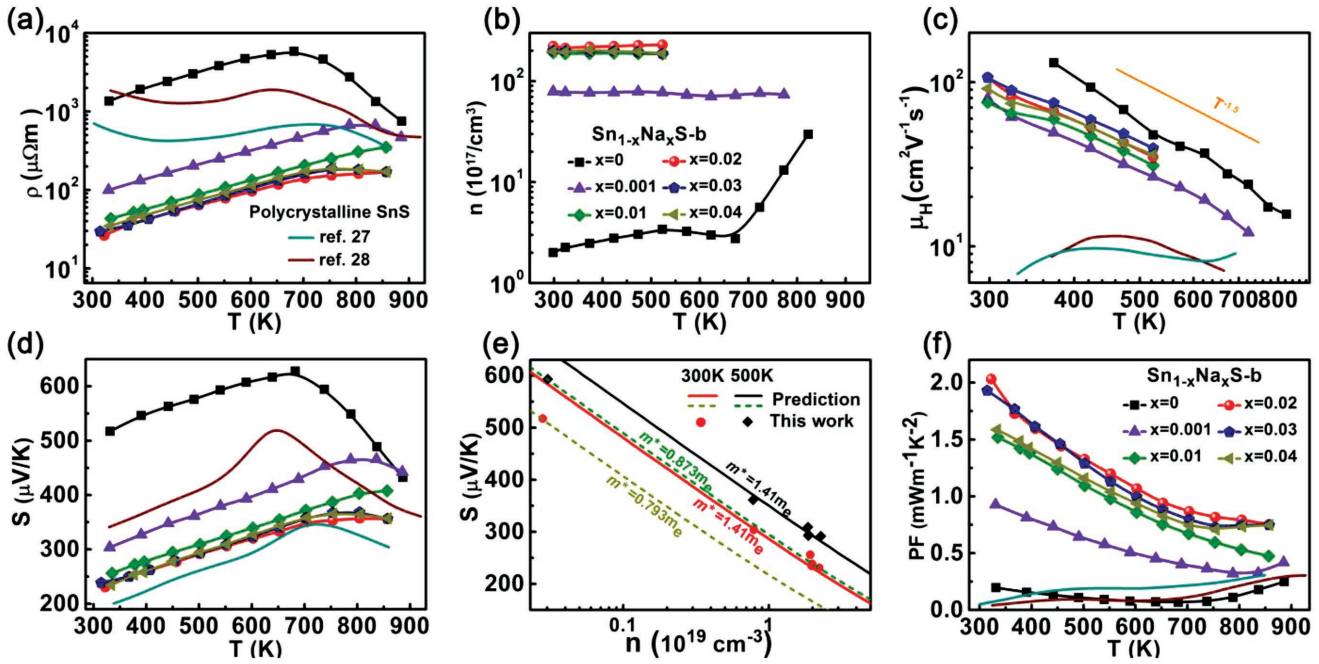

Figure 3. Temperature-dependent electronic properties of $Sn_{1-x}Na_xS$ ($x = 0$, 0.001, 0.01, 0.02, 0.03, and 0.04) single crystals along the crystallographic *b*-axis: a) electrical resistivity, b) Hall carrier concentration, c) Hall mobility, d) Seebeck coefficient, e) Pisarenko plot, and f) power factor. Data on the temperature-dependent transport properties reported for polycrystalline SnS doped with Na[34] and Ag[38] are shown for comparison.

to make a Pisarenko plot and further illustrate the behavior of electronic transport properties (detailed calculations are presented in the Supporting Information). As shown in Figure 3e, the experimental carrier concentration and the Seebeck coefficient fit well the Pisarenko line using the effective SPB model with different DOS effective masses. We found that the DOS effective mass guided by the navy dash line ($m^* = 0.793\ m_e$) fit the undoped sample ($\approx 2.0 \times 10^{17}$ cm^{-3}), and the dependence of Na-doped single crystal samples could be fit with $m^* = 1.41\ m_e$ at 300 K. By combining fitting with the DOS effective mass obtained from DFT calculations (see Table 1) and the shift of the Fermi level with different carrier concentration using the BoltzTrap code (Figure 2a), we speculated that the Fermi level would be above the valence band edge for the undoped sample, whereas the lower-lying heavy band began to contribute when the crystals were heavily doped with Na. To further validate this hypothesis, we performed fitting for experimental data at 500 K (Figure 3e). The DOS effective mass obtained from fitting slightly increased with temperature for the undoped sample. Furthermore, the Hall carrier concentration was consistent with the fitting result based on the SPB model, as listed in **Table 2**.

Figure 3 displays the temperature-dependent electronic properties of undoped and Na-doped SnS single crystals along the *b*-axis. The electrical resistivity (ρ), Figure 3a, of all crystals initially rose with the increasing temperature, showing a metallic behavior, reached a maximum, and then decreased. The temperature at which the resistivity reached its peak value shifted to higher temperatures as the carrier concentration increased. The eventual decrease in the resistivity was caused by the onset of intrinsic excitations. The magnitude of the electrical resistivity decreased sequentially with the increasing Na content (up to 2%), obviously because of the boosted carrier concentration upon doping. For instance, the Hall carrier concentration at 300 K was significantly enhanced from $\approx 2.0 \times 10^{17}$ cm^{-3} for the undoped SnS crystal to 2.3×10^{19} cm^{-3} for the $Na_{0.02}Sn_{0.98}S$ crystal (see Figure 3b). Note, however, that in comparison to the effect of Na doping in SnSe,[27] the doping efficiency of Na

Table 2. Room temperature carrier concentration obtained by different methods.

Fermi points	Fermi level [eV]	Calculation [cm^{-3}]	Samples $Na_xSn_{1-x}S$	SPB model [cm^{-3}]	Hall carrier concentration [cm^{-3}]
UN1	−0.26	5.0E17	$x = 0$	3.7E17	2.0E17
GZ1	0.0	8.5E18	$x = 0.001$	8.1E18	7.8E18
			$x = 0.01$	2.0E19	1.9E19
			$x = 0.02$	2.6E19	2.3E19
			$x = 0.03$	2.4E19	2.0E19
			$x = 0.04$	2.5E19	1.9E19
GA1	0.055	5.0E19			

© 2018 WILEY-VCH Verlag GmbH & Co. KGaA, Weinheim

in SnS was lower, and this may have limited further enhancements in the TE performance of SnS. The onset of intrinsic excitations is clearly seen in Figure 3b on the carrier concentration of pure SnS that underwent a rapid increase above 700 K. As shown in Figure 3c, the temperature dependence of the Hall mobility, calculated from $\mu_H = \rho^{-1} e^{-1} n_H^{-1}$, followed the $\mu \approx T^{-1.5}$ dependence, implying the dominance of acoustic phonon scattering. As expected, the Hall mobility for the undoped SnS crystal was higher than for the Na-doped SnS crystals over the whole temperature range. We attributed this higher mobility to allow scattering because of the mass difference and the atomic radii difference between Na and Sn. Compared with polycrystalline samples of SnS (≈10 $cm^2 V^{-1} s^{-1}$), the carrier mobility in our single crystals was greatly improved, which undoubtedly was the consequence of strongly diminished charge scattering by grain boundaries.

The positive values of the Seebeck coefficient shown in Figure 3d indicated that all crystals were p-type semiconductors. As expected, the Seebeck coefficient clearly diminished as the Hall carrier concentration increased. At elevated temperatures, the Seebeck coefficient turned over and decreased. This, again, is a distinct signature of the onset of intrinsic excitations at which point the minority electrons start to compensate the majority holes. The turn over shifted to higher temperatures as the carrier concentration of holes increased. Figure 3f presents the power factor of all SnS crystals. We achieved the maximum power factor of 2.0 mW $m^{-1} K^{-2}$ at room temperature in a SnS crystal doped with 2 at% Na. This value of the power factor was substantially higher than that of the pure SnS crystal (0.19 mW $m^{-1} K^{-2}$) and significantly exceeded the previously reported power factor of polycrystalline SnS samples.[34,38]

Thermal properties: **Figure 4**a,b displays the temperature-dependent total and lattice thermal conductivity along the *b*-axis direction for all single crystal samples. The total thermal conductivity (κ) of our crystals ranged from 2.36 to 2.87 W $m^{-1} K^{-1}$ at 320 K, which was higher than that for the SnSe single crystal along the same direction.[30] The total thermal conductivity of all SnS crystals decreased as the temperature increased. We attained the minimum value of 0.61 W $m^{-1} K^{-1}$ for the $Na_{0.02}Sn_{0.98}S$ single crystal along the *b*-axis at about 870 K. We obtained the lattice thermal conductivity (κ_L) of all samples by subtracting the electronic contribution (κ_e) from the total thermal conductivity, ($\kappa_L = \kappa - \kappa_e$). The electronic thermal conductivity contribution (κ_e) was calculated according to the Wiedemann–Franz law ($\kappa_e = L\ T\ \rho^{-1}$). Here, L is the Lorenz number, which is estimated based on the SPB model (see the Supporting Information). Comparing Figure 4a,b, it follows that the electronic thermal conductivity of all SnS crystals represented a minor fraction of the overall thermal conductivity. The lattice thermal conductivity exhibited a sharp downward trend closely following the T^{-1} law and indicating the dominance of phonon Umklapp scattering processes. We achieved the minimum lattice thermal conductivity of 0.54 W $m^{-1} K^{-1}$ at about 870 K for the 2 at% Na-doped single crystal. Apparently, the lattice thermal conductivity of all SnS crystals had an intrinsically low value at elevated temperatures because of the strong lattice anharmonicity associated with the large Grüneisen parameters (γ_a = 3.9, γ_b = 2.1, γ_c = 2.3).[35] We also observed comparably low lattice thermal conductivity values and large Grüneisen parameters for polycrystalline SnS.[32]

Figure of merit: **Figure 5**a displays the temperature-dependent dimensionless TE figure of merit (zT) for our $Sn_{1-x}Na_xS$ single crystals measured along the *b*-axis direction. The zT value of all SnS single crystals increased as the temperature rose in the entire temperature range, and the figure of merit also was enhanced by Na doping. The data in Figure 5a show that the highest zT value of ≈1.1 at ≈870 K was achieved for the SnS crystal with the Na content of $x = 0.02$. This value was higher than that of Na-doped lead(II) sulfide (PbS) with the same Na-doping content.[39] As shown in Figure S3 (Supporting Information) and Figure 5b, we compared the highest zT values and the average zT values obtained with our SnS single crystals to corresponding values of several representative metal sulfides except superionic conductors as reported in the previous literature. Clearly, our Na-doped SnS single crystals are among the best TE sulfides in terms of peak zT value as well as average zT. More important, the significant enhancement in the average zT (≈180%), compared with the SnS polycrystalline material, makes the Na-doped SnS single crystal more plausible for practical TE applications.[40,41] According to theoretical calculations,[35] a higher zT value (≈1.9 at 800 K) for SnS single crystal samples along the *b*-axis direction could be realized by combining improved doping efficiencies for the higher PF with the reduced total thermal conductivity via forming solid solutions.

Anisotropy: According to the characteristic layered structure of SnS and the experimental results (see the Supporting

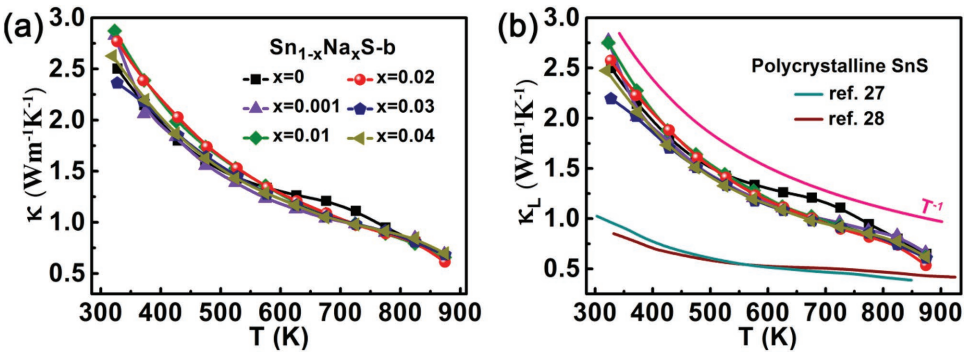

Figure 4. Temperature-dependent thermal transport properties of $Sn_{1-x}Na_xS$ (x = 0, 0.001, 0.01, 0.02, 0.03, and 0.04) single crystals along the crystallographic *b*-axis: a) the total thermal conductivity and b) the lattice thermal conductivity.

© 2018 WILEY-VCH Verlag GmbH & Co. KGaA, Weinheim

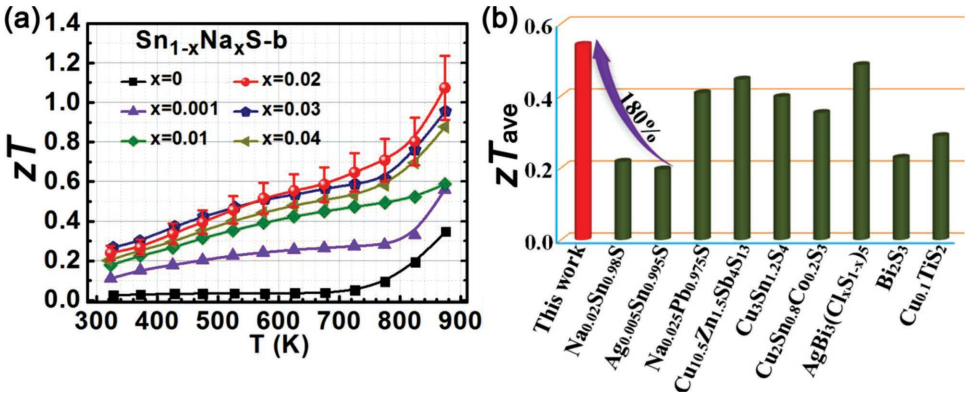

Figure 5. a) zT values for $Sn_{1-x}Na_xS$ (x = 0, 0.001, 0.01, 0.02, 0.03, and 0.04) single crystals along the crystallographic b-axis. b) The average value of zT for metal sulfides[34,38,39,42–47] in the temperatures range from ≈300 to ≈900 K. The detail methods[48] are displayed in the Supporting Information.

Information), we found that SnS single crystals exhibited strong textured character, indicating a strong anisotropy in the TE properties.[49,50] Thus, all transport properties should be measured along the same direction (Figure S1a, Supporting Information). Indeed, as shown in **Figure 6**, transport properties of pure SnS and $Na_{0.02}Sn_{0.98}S$ crystals displayed a strongly anisotropic character, with the electrical resistivity along the a-axis being much higher than that along the b-axis and the c-axis. With no obvious difference in the Seebeck coefficient measured at different directions, the PF along the a-axis clearly was less competitive than the other two directions. Additionally, the thermal conductivity along the a-axis for both SnS and $Na_{0.02}Sn_{0.98}S$ crystals was lower than the conductivity along the b-axis and the c-axis. This indicated a strongly anisotropic heat transport in the crystals, similar to that observed in SnSe.[26,27]

We prepared pristine and Na-doped SnS single crystals using a modified Bridgman method and studied their TE properties from room temperature to 873 K. We observed strong anisotropy in TE transport properties and identified the best performance along the b-axis. The grain boundary-free nature of the crystals gave rise to their higher mobility as compared with their polycrystalline counterpart. We found that Na-doping significantly increased the concentration of holes, which, in turn, enhanced the electrical conductivity, leading to a much-improved PF from 0.19 mW m^{-1} K^{-2} for the pure SnS crystal to 2.0 mW m^{-1} K^{-2} for the 2 at% Na-doped crystal. DFT calculations combined with the analysis based on the SPB model clearly verified the participation of the lower-lying heavy valence band in the transport process as a result of heavy Na doping. The participation of more than a single valence band benefited the Seebeck coefficient and the power factor. Strong anharmonicity of lattice vibrations and the highly anisotropic crystal structure of SnS maintained very low lattice thermal conductivity. Of all the single crystalline SnS samples, the maximum

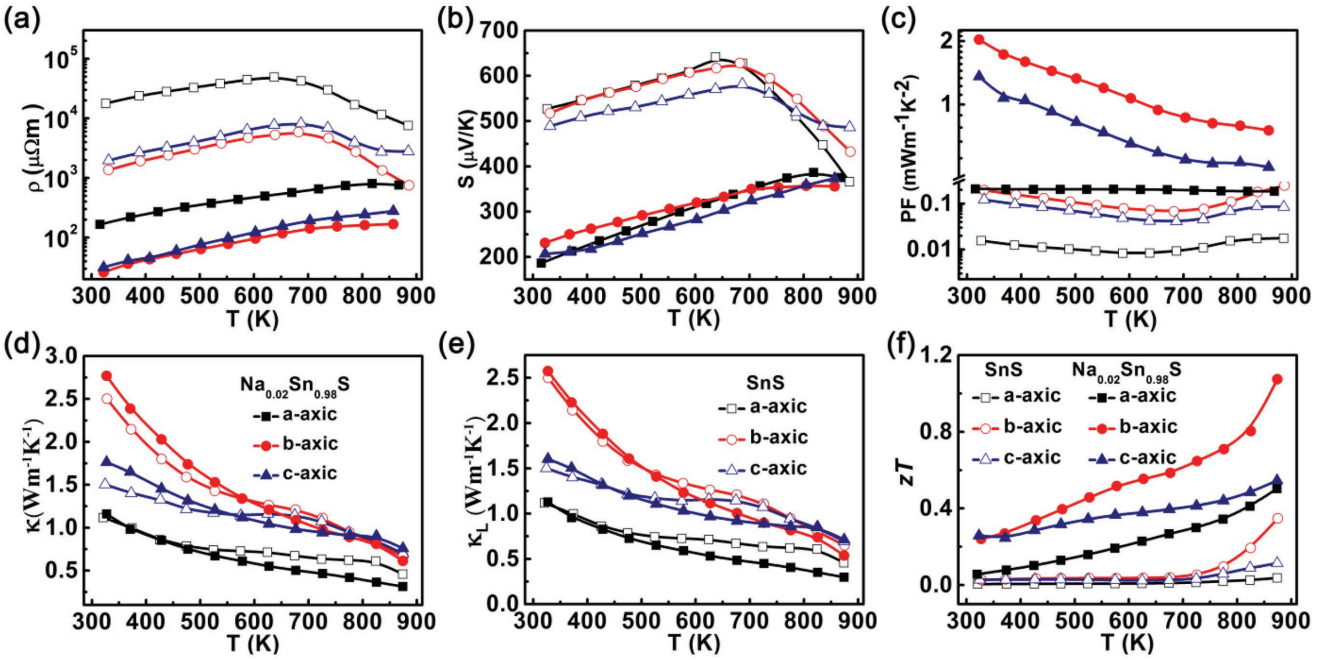

Figure 6. The anisotropic thermoelectric properties of $Na_{0.02}Sn_{0.98}S$ and SnS single crystals.

© 2018 WILEY-VCH Verlag GmbH & Co. KGaA, Weinheim

zT of 1.1 at 870 K was achieved in $Na_{0.02}Sn_{0.98}S$. This represented one of the highest zT values obtained for a metal sulfide-based TE material. Our results demonstrated that SnS single crystals consisting of inexpensive, earth-abundant, and nontoxic elements attained high TE performance. Therefore, these crystals are potential TE materials for power generation applications.

Experimental Section

Synthesis: Pure Sn granules (99.999%), S powder (99.99%), and Na chunks (99.9%) were weighed carefully according to the stoichiometry of $Sn_{1-x}Na_xS$ (x = 0, 0.001, 0.01, 0.02, 0.03, and 0.04) and the samples were loaded into cone-shaped quartz tubes under an argon atmosphere. The tubes were sealed under ≈5×10^{-4} Pa and placed them in another (larger diameter) quartz tube, which again evacuated and flame-sealed. This was done to protect the samples from oxidation as the cone-shaped quartz tube breaks easily when the crystal structure of SnS undergoes a phase transition from the *Cmcm* to the *Pnma* phase upon cooling. The tubes were heated slowly up to 1273 K over 20 h and soaked at that temperature for 15 h. Subsequently, the tubes were cooled to 1100 K as they were lowered at a rate of 1.5 mm h^{-1}. This carefully monitored process resulted in $Sn_{1-x}Na_xS$ single crystal ingots with a diameter of 14 mm and a height of 45 mm.[51]

Measurements: The obtained single crystal ingots were cut into ≈8.5 mm × 2 mm × 2 mm bars for electrical property measurements and square-shaped samples with dimensions of ≈6 mm × 6 mm × 1.5 mm to take thermal conductivity measurements along the three directions (along the *a*-, *b*-, and *c*-axis, respectively), as shown in Figure S1a (Supporting Information). The electronic transport property measurements were performed on a commercial system (LSR-3, Linseis) under a static helium atmosphere. The temperature-dependent Hall coefficient (R_H) was measured using a homemade apparatus. The thermal diffusivity (D) was measured using the LFA 457 (Netzsch, Selb, Germany) instrument and the heat capacity (C_p) was obtained through differential scanning calorimetry (404 F3, Netzsch), as shown in Figure S2 (Supporting Information). The thermal conductivity (κ) was calculated using $\kappa = \rho D C_p$, where ρ is the density (see Table S3 in the Supporting Information) measured by the Archimedes' method on a commercial instrument (BR-120N, Beyongtest). The estimated error in electrical resistivity, Seebeck coefficient, and thermal conductivity was about 5%, 7%, and 5%, respectively; and the overall uncertainty of zT was estimated at around 15% (error bars are displayed in the relevant figures). The crystal structures were determined using PANalytical X'pert apparatus (Netherlands) with CuKα radiation. The STEM and EDS mappings were performed at 300 kV on a probe-corrected FEI Titan G2 60–300 microscope (Hillsboro, OR, USA) with a super-X system. The bandgap was analyzed by ultraviolet–visible noninfrared spectrophotometer (UV-3600, Shimadzu, Kyoto, Japan).

DFT Calculations: The electronic band structure was computed within the framework of DFT using the Vienna ab initio Simulation Package,[52] in which the projector augmented plane wave[53] method was used for structure relaxation. The exchange–correlation function was defined using a generalized gradient approximation of Perdew–Burke–Ernzerhof.[54] The total energies were numerically converged to 1×10^{-6} eV using a basis set energy cutoff of 500 eV. The atomic positions were relaxed until the forces on the atoms were smaller than 0.01 eV $Å^{-1}$. For the Brillouin zone integrations, the Monkhorst–Pack k-mesh scheme was used with $3 \times 9 \times 9$ for the cell system.

Supporting Information

Supporting Information is available from the Wiley Online Library or from the author.

Acknowledgements

This work was financially supported in part by the National Natural Science Foundation of China (Grant Nos. 11674040, 11604032, 51472036, and 51672270), the Fundamental Research Funds for the Central Universities (106112016CDJZR308808). The work conducted at the Chongqing Institute of Green and Intelligent Technology, Chinese Academy of Sciences is also supported by Key Research Program of Frontier Sciences, CAS, Grant No. QYZDB-SSW-SLH016 and the Project for Fundamental and Frontier Research in Chongqing (CSTC2015JCYJBX0026).

Conflict of Interest

The authors declare no conflict of interest.

Keywords

electronic structure, SnS single crystal, SPB model, thermoelectrics

Received: January 8, 2018
Revised: March 6, 2018
Published online: April 6, 2018

[1] L. E. Bell, *Science* **2008**, *321*, 1457.
[2] M. S. Dresselhaus, G. Chen, M. Y. Tang, R. G. Yang, H. Lee, D. Z. Wang, Z. F. Ren, J. P. Fleurial, P. Gogna, *Adv. Mater.* **2007**, *19*, 1043.
[3] J. P. Heremans, M. S. Dresselhaus, L. E. Bell, D. T. Morelli, *Nat. Nanotechnol.* **2013**, *8*, 471.
[4] X. Lu, D. T. Morelli, Y. Wang, W. Lai, Y. Xia, V. Ozolins, *Chem. Mater.* **2016**, *28*, 1781.
[5] Q. Tan, J. F. Li, *J. Electron. Mater.* **2014**, *43*, 2435.
[6] G. J. Snyder, E. S. Toberer, *Nat. Mater.* **2008**, *7*, 105.
[7] T. Zhu, Y. Liu, C. Fu, J. P. Heremans, J. G. Snyder, X. Zhao, *Adv. Mater.* **2017**, *29*, 1605884.
[8] M. Zhou, G. J. Snyder, L. Li, L. D. Zhao, *Inorg. Chem. Front.* **2016**, *3*, 1449.
[9] K. F. Hsu, S. Loo, F. Guo, W. Chen, J. S. Dyck, C. Uher, T. Hogan, E. K. Polychroniadis, M. G. Kanatzidis, *Science* **2004**, *303*, 818.
[10] J. P. Heremans, C. M. Thrush, D. T. Morelli, *Phys. Rev. B* **2004**, *70*, 115334.
[11] O. Falkenbach, J. Tinz, A. S. Schulze, E. Mueller, S. Schlecht, *Phys. Status Solidi A* **2016**, *213*, 699.
[12] Z. W. Chen, B. H. Ge, W. Li, S. Q. Lin, J. W. Shen, Y. J. Chang, R. Hanus, G. J. Snyder, Y. Z. Pei, *Nat. Commun.* **2017**, *8*, 13828.
[13] S. I. Kim, K. H. Lee, H. A. Mun, H. S. Kim, S. W. Hwang, J. W. Roh, D. J. Yang, W. H. Shin, X. S. Li, Y. H. Lee, *Science* **2015**, *348*, 109.
[14] J. D. Wasscher, W. Albers, C. Haas, *Solid-State Electron.* **1963**, *6*, 261.
[15] S. Q. Lin, W. Li, X. Y. Zhang, J. Li, Z. W. Chen, Y. Z. Pei, *Inorg. Chem. Front.* **2017**, *4*, 1066.
[16] Y. Pei, L. Zheng, W. Li, S. Lin, Z. Chen, Y. Wang, X. Xu, H. Yu, Y. Chen, B. Ge, *Adv. Electron. Mater.* **2016**, *2*, 1600019.
[17] W. Yao, D. Yang, Y. Yan, K. Peng, H. Zhan, A. Liu, X. Lu, G. Wang, X. Zhou, *ACS Appl. Mater. Interfaces* **2017**, *9*, 10595.
[18] M. D. Nielsen, V. Ozolins, J. P. Heremans, *Energy Environ. Sci.* **2013**, *6*, 570.
[19] D. Yang, W. Yao, Y. Yan, W. Qiu, L. Guo, X. Lu, C. Uher, X. Han, G. Wang, T. Yang, X. Zhou, *NPG Asia Mater.* **2017**, *9*, e387.
[20] D. Yang, W. Yao, Q. Chen, K. Peng, P. Jiang, X. Lu, C. Uher, T. Yang, G. Wang, X. Zhou, *Chem. Mater.* **2016**, *28*, 1611.

 © 2018 WILEY-VCH Verlag GmbH & Co. KGaA, Weinheim

[21] Y. Z. Pei, A. D. LaLonde, N. A. Heinz, X. Y. Shi, S. Iwanaga, H. Wang, L. D. Chen, G. J. Snyder, *Adv. Mater.* **2011**, *23*, 5674.
[22] S. Bhattacharya, N. S. Gunda, R. Stern, S. Jacobs, R. Chmielowski, G. Dennler, G. K. H. Madsen, *Phys. Chem. Chem. Phys.* **2015**, *17*, 9161.
[23] Y. Z. Pei, X. Y. Shi, A. LaLonde, H. Wang, L. D. Chen, G. J. Snyder, *Nature* **2011**, *473*, 66.
[24] X. Lu, W. Yao, G. Wang, X. Zhou, D. Morelli, Y. Zhang, H. Chi, S. Hui, C. Uher, *J. Mater. Chem. A* **2016**, *4*, 170963.
[25] J. Yang, L. L. Xi, W. J. Qiu, L. H. Wu, X Shi, L. D. Chen, J. H. Yang, W. Q. Zhang, C. Uher, D. J. Singh, *npj Comput. Mater.* **2016**, *2*, 15015.
[26] L. D. Zhao, S. H. Lo, Y. Zhang, H. Sun, G. Tan, C. Uher, C. Wolverton, V. P. Dravid, M. G. Kanatzidis, *Nature* **2014**, *508*, 373.
[27] K. Peng, X. Lu, H. Zhan, S. Hui, X. Tang, G. Wang, J. Dai, C. Uher, G. Wang, X. Zhou, *Energy Environ. Sci.* **2016**, *9*, 454.
[28] T. Duong, V. Q. Nguyen, G. Duvjir, V. T. Duong, S. Kwon, J. Y. Song, J. K. Lee, J. E. Lee, S. Park, T. Min, J. Lee, J. Kim, S. Cho, *Nat. Commun.* **2016**, *7*, 13713.
[29] L. D. Zhao, G. J. Tan, S. Q. Hao, J. Q. He, Y. L. Pei, H. Chi, H. Wang, S. K. Gong, H. B. Xu, V. P. Dravid, C. Uher, G. J. Snyder, C. Wolverton, M. G. Kanatzidis, *Science* **2016**, *351*, 141.
[30] K. L. Peng, B. Zhang, H Wu, X. L. Cao, A. Li, D. F. Yang, X. Lu, G. Y. Wang, X. D. Han, C. Uher, X. Y. Zhou, *Mater. Today*, https://doi.org/10.1016/j.mattod.2017.11.005.
[31] J. S. Rhyee, K. H. Lee, S. M. Lee, E. Cho, S. I. Kim, E. Lee, Y. S. Kwon, J. H. Shim, G. Kotliar, *Nature* **2009**, *459*, 965.
[32] R. Guo, X. Wang, Y. Kuang, B. Huang, *Phys. Rev. B* **2015**, *92*, 115202.
[33] B. Z. Sun, Z. Ma, C. He, K. Wu, *RSC Adv.* **2015**, *5*, 56382.
[34] B. Zhou, S. Li, W. Li, J. Li, X. Zhang, S. Lin, Z. Chen, Y. Pei, *ACS Appl. mater. Interfaces* **2017**, *9*, 34033.
[35] S. Hao, V. P. Dravid, M. G. Kanatzidis, C. Wolverton, *APL Mater.* **2016**, *4*, 104505.
[36] G. K. H. Madsen, D. J. Singh, *Phys. Commun.* **2006**, *175*, 67.
[37] G. Ding, G. Gao, K. Yao, *Sci. Rep.* **2015**, *5*, 9567.
[38] Q. Tan, L. D. Zhao, J. F. Li, C. F. Wu, T. R. Wei, Z. B. Xing, M. G. Kanatzidis, *J. Mater. Chem. A* **2014**, *2*, 17302.
[39] L. D. Zhao, J. He, S. Hao, C. I. Wu, T. P. Hogan, C. Wolverton, V. P. Dravid, M. G. Kanatzidis, *J. Am. Chem. Soc.* **2012**, *134*, 16327.
[40] G. Tan, L. D. Zhao, M. G. Kanatzidis, *Chem. Rev.* **2016**, *116*, 12123.
[41] L. Yang, Z. G. Chen, M. S. Dargusch, J. Zou, *Adv. Electron. Mater.* **2017**, *8*, 1701797.
[42] X. Lu, D. T. Morelli, Y. Xia, F. Zhou, V. Ozolins, H. Chi, X. Zhou, C. Uher, *Adv. Energy Mater.* **2013**, *3*, 342.
[43] Y. Yang, P. Ying, J. Wang, X. Liu, Z. Du, Y. Chao, J. Cui, *J. Mater. Chem. A* **2017**, *5*, 18808.
[44] H. W. Zhao, X. X. Xu, C. Li, R. M Tian, R. Z. Zhang, R. Huang, Y. Lu, D. X. Li, X. H. Hu, L. Pan, Y. F. Wang, *J. Mater. Chem. A* **2017**, *5*, 23267.
[45] G. Tan, S. Hao, J. Zhao, C. Wolverton, M. G. Kanatzidis, *J. Am. Chem. Soc.* **2017**, *139*, 6467.
[46] K. Biswas, L. D. Zhao, M. G. Kanatzidis, *Adv. Energy Mater.* **2012**, *2*, 634.
[47] E. Guilmeau, Y. Bréard, A. Maignan, *Appl. Phys. Lett.* **2011**, *99*, 052107.
[48] K. L. Peng, H. Wu, Y. C. Yan, L. J. Guo, G. Y. Wang, X. Lu, X. Y. Zhou, *J. Mater. Chem. A* **2017**, *5*, 14053.
[49] Asfandiyar, T. R. Wei , Z. Li, F. H. Sun, Y. Pan, C. F. Wu, M. U. Farooq, H. Tang, F. Li, B. Li, J. F. Li, *Sci. Rep.* **2017**, *7*, 43262.
[50] M. M. Nassary, *J. Alloys Compd.* **2005**, *398*, 21.
[51] W. Albers, C. Haas, F. van der Maesen, *J. Phys. Chem. Solids* **1960**, *15*, 306.
[52] G. Kresse, J. Furthmuller, *Phys. Rev. B* **1996**, *54*, 11169.
[53] G. Kresse, D. Joubert, *Phys. Rev. B* **1999**, *59*, 1758.
[54] J. P. Perdew, K. Burke, M. Ernzerhof, *Phys. Rev. Lett.* **1996**, *77*, 3865.

© 2018 WILEY-VCH Verlag GmbH & Co. KGaA, Weinheim